

Stress, occurrence rates and b -value on the Nankai megathrust system inferred from earthquake simulation

Rodolfo Console^{1,2}, Roberto Carluccio¹ and Paola Vannoli¹

¹Istituto Nazionale di Geofisica e Vulcanologia, Rome 00143, Italy. E-mail: Rodolfo.console@ingv.it

²Center of Integrated Geomorphology for the Mediterranean Area, Rodolfo Console, Potenza 85100, Italy

Accepted 2025 January 21. Received 2024 November 6; in original form 2024 May 1

SUMMARY

We aim to improve our comprehension of the seismic process and to identify possible long-term predictability tools of strong earthquakes through the simulation performed by a new-generation simulator code based on a well-elaborated model of the earthquake sources. We applied our previously tested physics-based earthquake simulator to the Nankai megathrust fault system, characterized by a 13 centuries historical record of strong earthquakes. Our results show these significant seismicity patterns characterizing the seismic cycles: the average stress increases almost linearly, while its standard deviation decreases more and more rapidly as the next major earthquake approaches; the coseismic stress drop and the simultaneous increase of the standard deviation mark the beginning of the new seismic cycle; and the b -value tends to increase some decades before major earthquakes and exhibits correlation with the occurrence rate. Our results encourage further investigations about the application of simulators in support of other methodologies of earthquake forecasting.

Key words: Japan; Finite element method; Numerical modelling; Probabilistic forecasting; Seismicity and tectonics; Statistical seismology.

1 INTRODUCTION

After more than 120 yr of unsuccessful efforts, seismologists are still very far from achieving any kind of reliable and applicable method of earthquake prediction based on short-term precursors. A comprehensive review of the present situation has been very clearly given by Rundle *et al.* (2022).

In the absence of deterministic earthquake prediction tools, statistical methods based on information about past earthquakes are applied to earthquake hazard assessment. The simplest statistical model is given by the space-variable, time-independent Poisson hypothesis, also referred to as the background seismicity. This is the most frequently adopted model for disaster mitigation measures by Governments all over the World. However, it is widely recognized that earthquake occurrence rates are variable in both short and long terms. Short-term features are commonly named foreshock and aftershock sequences, clusters and swarms. This kind of behaviour may be quantitatively described by the Epidemic Type Aftershock Sequence model, which has become quite popular in the seismological literature starting from the initial steps of Ogata (1998), Console & Murru (2001) and Console *et al.* (2003), followed by many others.

In this paper, we are mainly concerned with time-dependent long-term features of strong earthquakes, based on the elastic rebound theory introduced by Reid (1910) upon evidence obtained from the 1906 San Francisco Earthquake. The statistical models describing

the inter-event time distribution of large earthquakes entirely rupturing a seismogenic fault belong to the category of renewal models and are characterized by two free parameters. They allow the calculation of the occurrence probability of the next earthquake, once the two free parameters and the time elapsed from the latest characteristic earthquake are known or inferred. However, the limited availability of long historical or palaeoseismic records with individually dated ruptures, combined with uncertainties in data and parameters, makes it challenging to determine the form of the recurrence distribution. For instance, even in a country like Japan, which owns a historical record of earthquakes longer than 1000 yr, it is likely that the seismic catalogue does not capture all possible longer inter-event times. In some cases, palaeoseismic information could help address this question. Anyway, even palaeoseismological information does not span a period encompassing more than a few large earthquakes, allowing a robust statistical analysis (e.g. Mosca *et al.* 2012).

Starting from the pioneering work of Rundle & Jackson (1977), Rundle & Brown (1991) and Ward 1992, physics-based earthquake simulators have received growing attention as a tool for developing and testing hypotheses of the earthquake process, and justifying earthquake observations. Among these observations, there are well-known statistical relationships like magnitude–frequency distributions, temporal relationships like the Omori law, and some properties of earthquake clustering. Earthquake simulators may address the typical limitations existing in real observations, such as

completeness, homogeneity and duration, enabling the evaluation of various seismogenic process models and the application of renewal models (Ward 1996, 2000, 2012; Tullis 2012; Wilson *et al.* 2017; Console *et al.* 2018, 2020, 2022a,b, 2023; Shaw *et al.* 2018).

Even if the most complex earthquake simulators remain models approximating the infinitely more complex physical reality of the earthquake process, and not all conclusions based on this kind of models can be tested in any detail against actual earthquakes, there is a wide consensus on their usefulness for improving overall testing procedures of earthquake forecasting (e.g. Field 2015, 2019; Schultz *et al.* 2015; Christophersen *et al.* 2017; Rundle *et al.* 2022).

In this study, we applied a previously tested physics-based earthquake simulator to the Nankai megathrust fault system, a well-known seismogenic zone, characterized by both a high rate of strong earthquakes and a long historical record spanning about 13 centuries (e.g. Kanamori 1972; Ando 1975a,b; Ishibashi 1981; Kato 1983; Sykes & Menke 2006; Parsons *et al.* 2012; Fitzenz 2018; Fujiwara *et al.* 2023). We produced a long-term simulated catalogue lasting 1000 yr and containing more than 17 600 $M_w > 5.0$ earthquakes, attempting to mimic observed seismic features such as the frequency–magnitude distribution, the pseudo-periodicity of major ruptures and their inter-event time in the seismic cycle, along with some possible long-term precursory patterns. Our simulator is based on an algorithm constrained by several physical faulting and source parameters, and includes some heuristic rules controlling the nucleation, growth and stopping of the rupture of a seismogenic source (Console *et al.* 2023). Our results show interesting seismic features characterizing the behaviour of the seismic process on single fault segments. We believe that identifying these features could be a key to modelling the occurrence of future damaging earthquakes, and a contribution to the ambitious task of earthquake forecasting.

2 THE NANKAI MEGATHRUST FAULT SYSTEM

In southwestern Japan, along the Nankai Trough subduction zone, the Philippine Sea oceanic plate is subducting beneath the Eurasian/Amur continental plate at a horizontal velocity of ca. 5–6 cm yr⁻¹ (Zang *et al.* 2002; DeMets *et al.* 2010).

The Nankai megathrust fault system is a well-known seismogenic structure 700 km long, aligned with the Pacific Ocean coast, which generated several earthquakes of magnitude larger than 8.0 in the last 13 centuries (Table 1). Therefore, megathrust earthquakes have occurred repeatedly at intervals of 100–150 yr along the Nankai Trough, and are believed to occur along the plate interface, between the over-riding continental plate and the subducting oceanic plate (e.g. Noda *et al.* 2021; Saito & Noda 2022; Yamamoto *et al.* 2022). The largest interplate earthquake occurred in the source region of the 1944 earthquake (M_w 8.2) was the M_w 6.5 earthquake on 2016 April 1 (Nakano *et al.* 2018a). Instead, the largest and the second largest intraplate earthquakes observed in this region were the M 7.4 and M 7.1 events on 2004 September 5.

The Nankai Trough fault system is typically modelled as subdivided into five main fault segments (Fig. 1 and Table 2; e.g. Ando 1975a, b; Parsons *et al.* 2012; Fujiwara *et al.* 2023). This partition is mainly based on studies of the source mechanisms of historical earthquakes and the forearc submarine topography, which reflects the seismotectonic activities. Each of the five fault segments has a length of 100–150 km along the trough axis and almost corresponds to the distribution of forearc basins (e.g. Fujiwara *et al.* 2023, and

Table 1. Historical and instrumental mega-earthquakes that ruptured more segments of the Nankai megathrust (modified from Ando 1975a, b; Parsons *et al.* 2012, and references therein).

Date	M	Causative faults				
684 November 29	8.4	AB	or	ABCD	or	ABCDE
887 August 26	8.6	AB	or	ABC		
1096 December 17	8.4	CD	or	CDE		
1099 February 22	8.4	AB				
1361 August 3	8.4	AB	or	ABCD	or	ABCDE
1498 September 20	8.6	CDE	or	ABCDE		
1605 February 3	7.9	ABCD				
1707 October 28	8.4	ABCDE				
1854 December 23	8.4	CDE				
1854 December 24	8.4	AB				
1944 December 7	8.2	CD				
1946 December 20	8.2	AB				

reference therein). These five segments are characterized by different slip rates and can rupture separately from or simultaneously with each other (Table 1 and Fig. 1).

Note that the most recent large earthquakes, the 1944 December 7 and 1946 December 20 earthquakes (both of magnitude 8.1), ruptured adjacent segments of the subduction zone, and some investigators suggest that this boundary is associated with a physical barrier to rupture that can be due to change in the dip of the plate interface (e.g. Baba & Cummins 2005). In any case, it is believed that this barrier may have been crossed during some historical earthquakes (Table 1). Note that no large earthquake listed in Table 1 is caused by the rupture of a single segment, while the pairs of segments A–B and C–D are always associated in a unique event. Moreover, Table 1 does not exhibit a clear correlation between the magnitude of single earthquakes and the size of the ruptured area. For instance, the smallest magnitude (7.9) is attributed to the 1605 earthquake, which is supposed to have ruptured the four segments from A to D, while a magnitude of 8.4 is attributed to the earthquakes of 1854, reported as having ruptured only segments A and B. These discrepancies may be explained by the uncertainties in magnitude estimates of historical earthquakes, as well as by the debated association of earthquakes to specific segments, most probably obtained from the memories of the severity of damages caused on the affected areas and the tsunami's effects. This issue will be dealt with in connection with the results of our simulation, which show that earthquakes of magnitude larger than 7.9 are not necessarily earthquakes caused by the full rupture of two or more segments.

Recent observations have shown that strain (stress) during an interseismic period (the time period between a strong Nankai Trough earthquake and the subsequent strong earthquake) is released not only by ordinary earthquakes but also by other phenomena. The

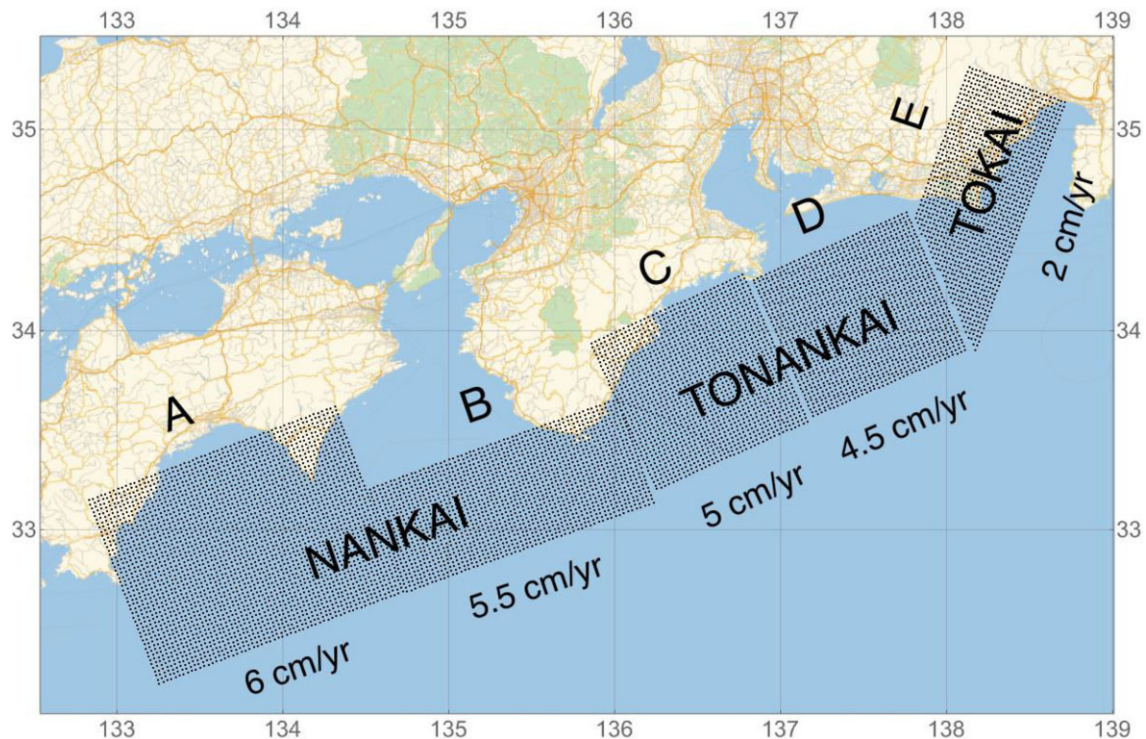


Figure 1. Surface projection of the Nankai megathrust seismogenic model. The seismogenic fault system is modelled by five quadrilateral faults conventionally labelled A–E from west to east, each of which is composed of square cells of $2.5 \text{ km} \times 2.5 \text{ km}$ (see Table 2 for their geometric and seismologic parameters; from Console & Carluccio 2021).

Table 2. Parameters of the seismogenic sources of the Nankai fault systems adopted in the simulator algorithm. The coordinates refer to the upper left edge of the fault as observed from the hangingwall.

Segment	Name	Lon (°)	Lat (°)	Minimum depth (km)	Strike (°)	Dip (°)	Rake (°)	Length (km)	Width (km)	Slip rate (mm yr^{-1})
A	Nankai	134.74	32.68	0.0	250	20	117	150	120	60
B	Nankai	136.25	33.13	0.0	250	25	117	150	70	55
C	Tonankai	137.18	33.54	3.0	245	24	113	95	100	50
D	Tonankai	138.13	33.90	3.0	245	32	113	95	100	45
E	Tokai	138.73	35.14	2.0	198	34	71	150	70	20

latter phenomena include spatiotemporal changes in plate coupling (slip deficit rates, e.g. Yokota *et al.* 2016; Nanjo & Yoshida 2018; Nakano *et al.* 2018a; Noda *et al.* 2021) as well as slow slip events (e.g. Araki *et al.* 2017; Yokota & Ishikawa 2020; Nanjo *et al.* 2024) and other slow earthquake activities (e.g. Nakano *et al.* 2018b). These phenomena play a pronounced role in the accumulation and release of strain (stress) around the Nankai Trough plate interface. Our simulator algorithm does have the option of choosing a different value of the coupling coefficient (cf) for each fault segment of the input source model. However, as further discussed in the following sections, we preferred to adopt a coefficient of 1.0 (full coupling) for the Nankai Trough fault system according to Scholz & Campos (2012). As a consequence, the simulator does not make a distinction if the events in the output catalogue should be called real earthquakes, slow earthquakes, or very slow slip events.

3 THE SIMULATOR ALGORITHM

We used the latest version of our simulator algorithm, described in detail by Console *et al.* (2015, 2018, 2020, 2022a, b, 2023, 2024).

Table 3. Features of the 1000 yr simulated catalogue

Number of earthquakes of $M \geq 5.2$	9204
Maximum-likelihood b -value ($M \geq 5.2$)	1.109 ± 0.008
Number of earthquakes of $M \geq 7.0$	69
Largest magnitude	8.63
Annual seismic moment M_0 ($M \geq 4.0$)	$1.51\text{E} + 20 \text{ N}\cdot\text{m yr}^{-1}$

Here, we recall that this algorithm is constrained by several physical and empirical elements:

- the geometry, source mechanism and average slip rate for every fault,
- modelling the process of rupture growth and termination by a set of heuristic rules, and
- interaction between earthquakes, with the Coulomb stress transfer computation.

There have been modifications and improvements in various versions of the simulator code. As far as the most recent versions are concerned, version 8 included the R&S constitutive law (Dieterich 1994; Console *et al.* 2022a), while version 9, adopted for this study, excludes such constitutive law, but includes a new free parameter

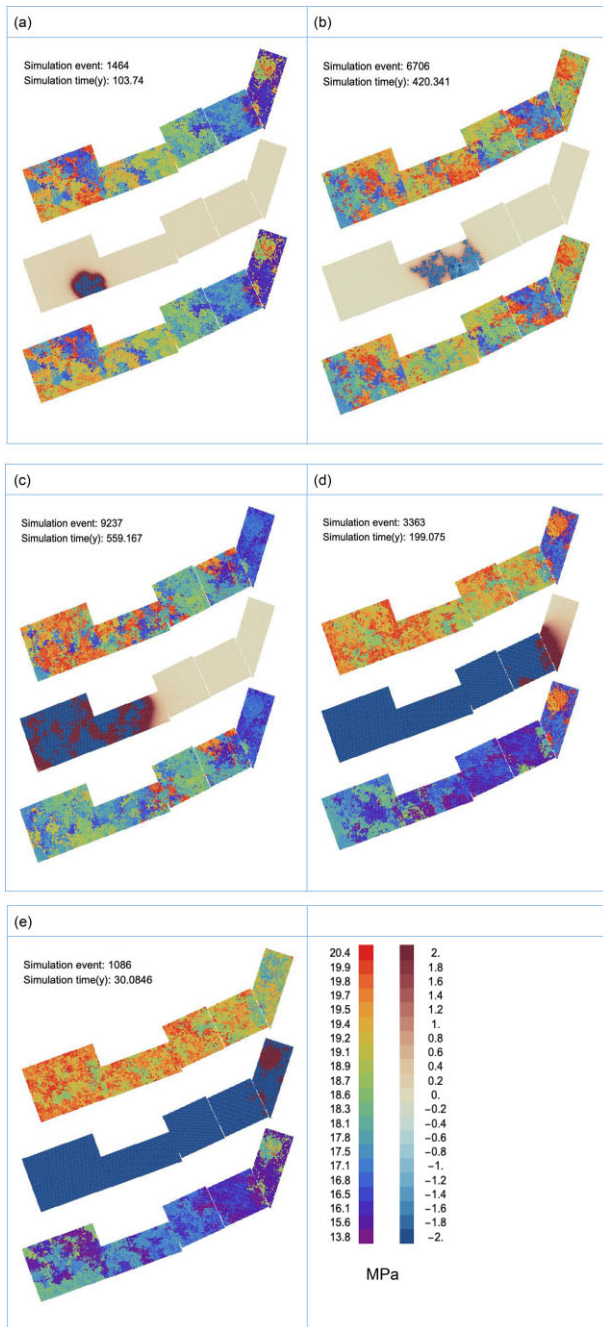


Figure 2. In each panel, from top to bottom, initial stress, stress drop and final stress for five earthquakes of different magnitudes on the Nankai megathrust fault system. (a) M 7.03; (b) M 7.61; (c) M 8.09; (d) M 8.58 and (e) M 8.63. The two labelled bars, respectively, show the stress before and after the earthquake and its stress drop. It is notable that the stress drop in panel (c) appears rough, while the stress drop in panel (d) looks smooth. It depends on the circumstance that the stress available in (c) prior to the rupture was not uniform (with the presence of areas of low stress), while in the other case it was almost uniformly close to the threshold.

by means of which the user may enhance the capability of a rupture to grow after nucleation (Console *et al.* 2022b, 2024).

The seismogenic system is modelled by quadrilateral fault segments, each of which is composed of many square cells of the same size. The main reason that suggested the adoption of this model

constituted by five segments was related to the necessity of assigning to these segments the different values of the slip rate shown in Section 2. The five quadrilateral fault segments that represent the Nankai seismogenic structures shown in Fig. 1 were discretized in cells of $2.5 \text{ km} \times 2.5 \text{ km}$. The minimum magnitude generated by an earthquake rupturing a single cell is 4.7 (not reported in the simulated catalogue).

Each cell is randomly assigned an initial stress budget, included in a fixed range. The stress is increased linearly in time according to the tectonic slip rate of the model. The earthquakes are initiated one by one on the cell with the largest stress budget, but only if it exceeds a given stress threshold. The second ruptured cell of the specific earthquake is chosen as that of largest stress budget among the eight cells surrounding the nucleation cell, and so on for the next ruptured cells, until the stopping condition is met, when none of the cells, including and surrounding the cells previously ruptured in the same earthquake, has a stress budget exceeding the threshold. Whenever a cell is ruptured, its slip is computed by means of a simple physical equation assuming a constant stress drop (in our case equal to 3.3 MPa), and part of its stress is transferred to the surrounding ones according to their distance and source mechanism. At the end of an earthquake, the average slip on the ruptured cells is computed, allowing the calculation of the seismic moment and the magnitude of earthquake through well-known relations.

The time interval spanned by the simulated catalogue was 1000 yr, excluding a warm-up period of 500 yr introduced to lead the system to a standby status, independent of the initial stress randomly assigned to every cell.

In our simulation, an earthquake of a given magnitude produced by the simulation algorithm could have ruptured only part of a single fault segment, or encompass more than one segment, without any constraint imposed by the size of the fault segment where the nucleation is started. This is related to the specific geometry of our Nankai Trough fault system, with a very short distance between the edges of two adjacent segments (Fig. 1). In this way, the stress released by ruptured cells is transferred between cells of different segments nearly as if they were a unique segment.

As for any other earthquake simulator, our algorithm is based on a great simplification of the extremely complex real earthquake process. In this respect, we proceeded according to the Occam principle that ‘the simpler the better’. For instance, our simulator does not make any difference between source mechanisms and hypocentral depths. However, as shown by previous applications of the same simulation code, our model mimics fairly well real seismic features, such as the pseudo-periodicity of strong earthquakes and the G-R magnitude distribution of earthquakes, with a substantial similitude to the characteristic earthquake model for strong earthquakes (Console *et al.* 2022b, 2024). In particular, Console *et al.* (2024) showed that the application of our simulator to different seismogenic areas as the central-northern Apennines and the Nankai–Tokai Trough, besides the strong differences in their time and size scales, produces substantial similarities in the respective earthquake patterns.

4 APPLICATION OF THE SIMULATOR

We ran the simulator for 1500 yr including a warm-up period of 500 yr. The 1000 yr output simulated catalogue contains 17 600 earthquakes of magnitude ranging from 5.03 (earthquakes rupturing only two cells) to 8.63 (an earthquake rupturing 9316 cells of the full fault system of segments A–E). Table 3 displays some of the main features of the simulated catalogue.

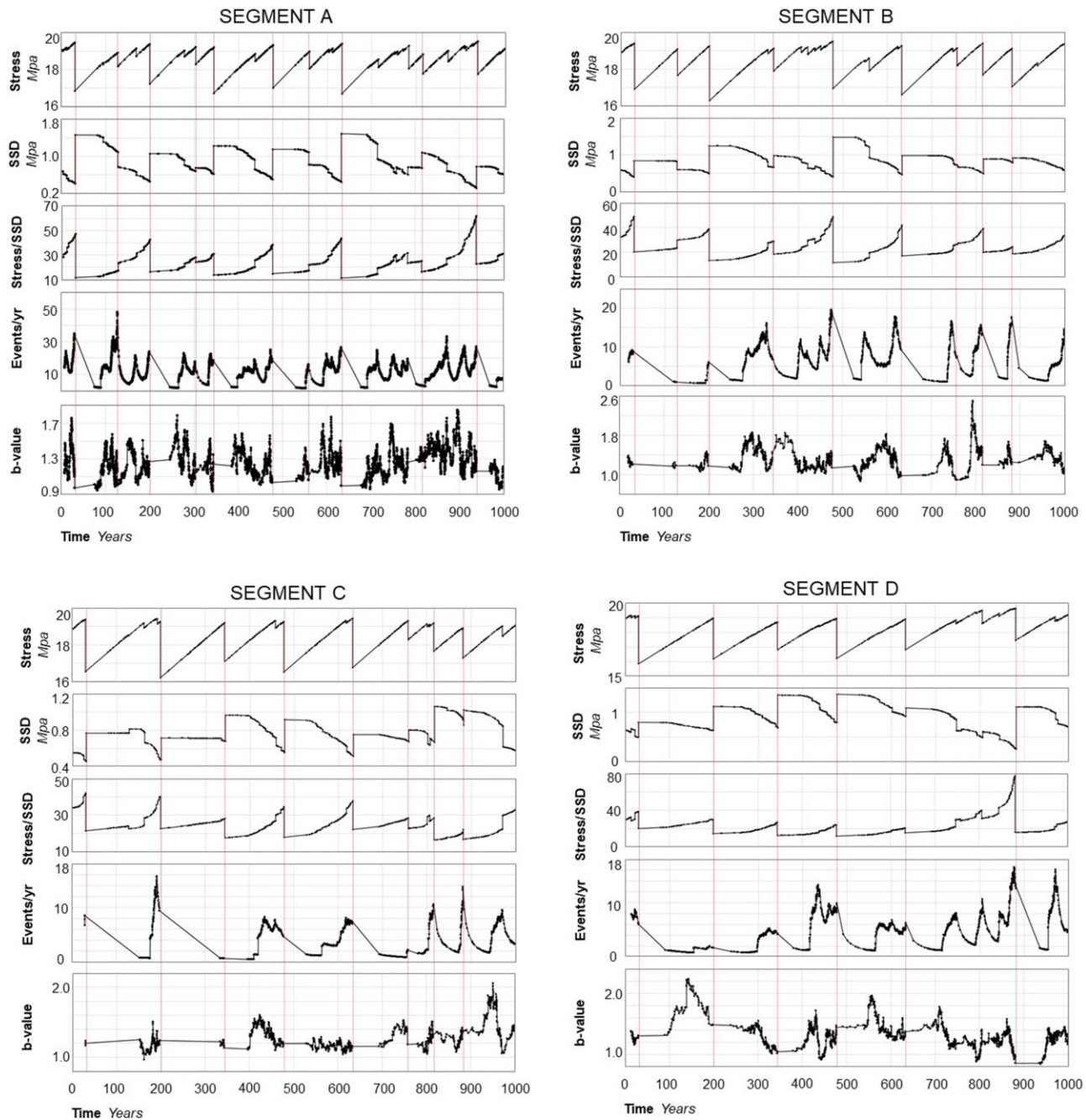


Figure 3. From top to bottom, for each of the A/B/C/D/E segments, time history of (1) average stress computed on all the cells; (2) SSD on the cells of each segment computed at the same time as in (1); (3) ratio between the average stress and its standard deviation computed at the same time as in (1); (4) occurrence rate on time windows of 100 earthquakes shifted by 10 earthquakes at each step and (5) b -value on time windows of 100 earthquakes shifted by 10 earthquakes at each step. Vertical lines indicate the occurrence time of earthquakes whose ruptures significantly modified the stress of one or more segments. The stress increase is due mostly to tectonic loading, but also to stress transfer from the cells of a segment to the others. The average stress drops at the time of each earthquake according to the size of the rupture on the specific segment participating in the earthquake. The standard deviation decreases (i.e. the stress becomes more uniform) approaching the occurrence time of earthquakes. The ratio between the values of the average stress and its standard deviation increases always and only before a strong earthquake, as a possible precursor of large-size earthquakes.

A comparison between the magnitude distributions of the simulated catalogue with that of real observations is unfeasible because it is not possible to distinguish in real catalogues the earthquakes occurring on the Nankai subduction fault system from all the earthquakes occurring close but outside of it. Moreover, very few interplate earthquakes occur during the inter-event period between two main shocks. A search of the International Seismological Centre

(2024) earthquake catalogue since 1970, for the region containing the fault system considered in our study, returned 164 $M 4.0 +$ earthquakes and only 5 $M 5.2 +$ earthquakes, with a maximum-likelihood b -value equal to 1.13, without distinguishing between interplate or intraplate earthquakes (see Figs A1 and A2 in Appendix A). This very low seismic activity can be explained by (i) the presence of activity in terms of the previously mentioned slow seismic events and

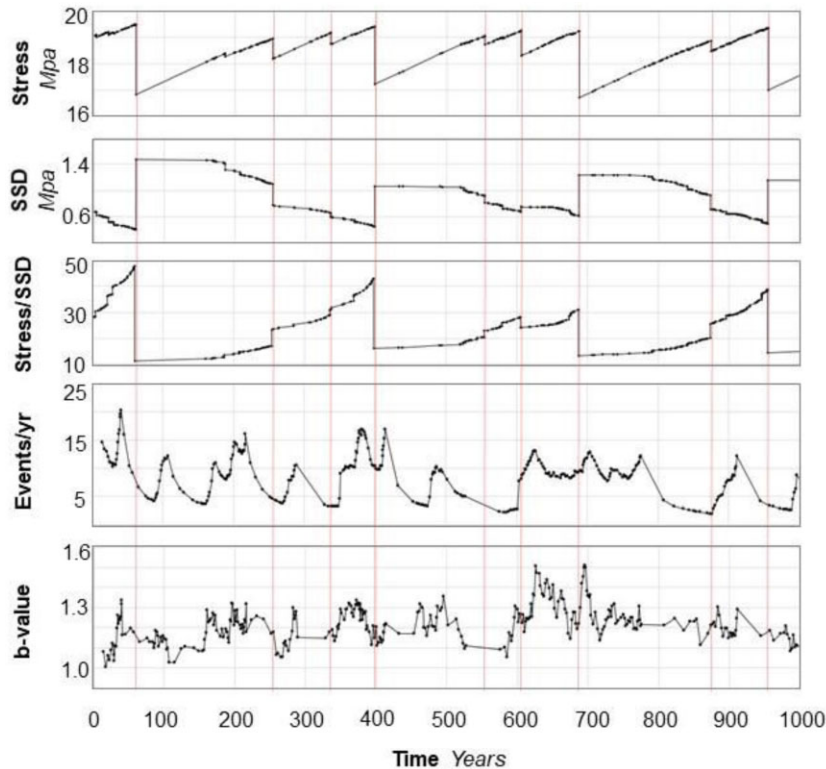


Figure 4. As in Fig. 3, for the case when the coupling coefficient for segment A is set equal to 0.5.

creeping not included in the ISC catalogue, and/or (ii) the present blockage of large asperities of the Nankai–Tokai fault system with accumulation of slip deficit, which will be released in the next strong earthquakes.

4.1. Stress variations in the earthquake cycle

As the simulator algorithm allows computing the stress on all the cells constituting the seismogenic structure adopted in the model, we may build up the stress history on each cell and display it in a sort of animation (Fig. 2).

In Fig. 2, we can note that before large magnitude earthquakes, stress is generally high and uniform. The rupture releases much stress in a non-uniform way on the source. In order to better study these features, we analysed the variations of the average stress and its standard deviation on single segments.

4.2. Time variations of stress, occurrence rate and b -value

Fig. 3 shows (in the first panel from the top) the average stress computed on all the cells of each fault segment from A to E in a time span of 1000 yr. Vertical red lines indicate the occurrence time of earthquakes whose ruptures significantly modified the stress of one or more segments. The stress increase is due mostly to tectonic loading, but also to stress transfer from the cells of a segment to the cells of the neighbouring segments. The average stress drops at the time of each earthquake according to the size of the rupture on the specific segment participating in the earthquake (equal to 3 MPa on every ruptured cell). It is worth to note that the stress reported on the y -axis of these plots must be considered just in a relative way,

as 20 MPa was the arbitrary choice for the value of the strength to be exceeded for rupturing a cell.

Fig. 3 also shows (in the second panel from the top) the standard deviation of stress (SSD) on the cells of each segment from A to E, computed at the same times as for the stress in the first panel. Moreover, the same figures also show (in the third panel from the top) the ratio between the values of the average stress and its standard deviation. This parameter increases always and only before a strong earthquake. We cannot provide a comparison of these features exhibited by the simulated catalogues with real observations. However, a change in the size of asperities on a seismic fault during the seismic cycle can be explained by a simple model of seismic coupling that connects asperity size, earthquake size and tectonic stress introduced by Ruff & Kanamori (1983). Another study putting in relation the size of asperities along fault zones with different stress regimes was published by Tormann *et al.* (2014). Assuming that the trend shown in Fig. 3 before large earthquakes (i.e. stress becomes higher and more uniform on a relevant patch of the fault system) is a phenomenon that happens in reality, it could be regarded as a promising tool for forecasting strong earthquakes. Unfortunately, it is not feasible to map the stress on the fault surface with the necessary resolution in the real environment. However, some seismicity patterns observable by means of modern high-quality seismic networks, such as spatiotemporal changes of occurrence rates b -values, could be associated with stress variation in the crust and applied in an operational forecasting system (Gulia *et al.* 2016; Montuori *et al.* 2016; Gulia & Wiemer 2019; Stallone & Marzocchi 2019).

In order to show possible relationships between stress and observable seismological features in our simulated catalogue, we developed a specific computer code for assessing the occurrence rate and

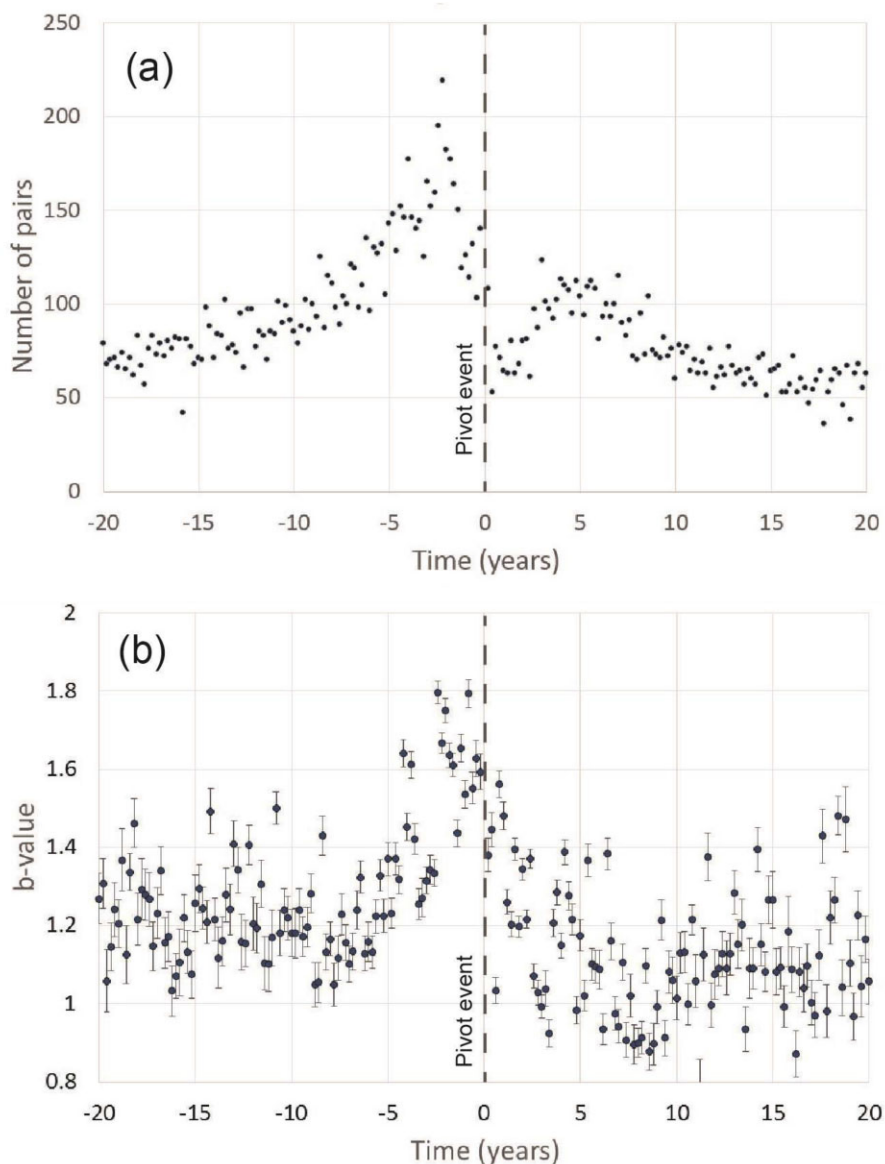


Figure 5. (a) Results of the stacking procedure described in the text, for the occurrence rate of earthquakes before and after earthquakes of $M \geq 5.8$. (b) As in (a) for the b -values.

the b -value in moving windows of a given number of earthquakes in the analysed catalogue. In this case, we chose a moving window of 100 earthquakes, shifted by 10 earthquakes at a time. There is an overlapping of 90 earthquakes between consecutive windows, and the time of the obtained parameters is the occurrence time of the last earthquake event of each window.

Fig. 3 shows the plots of occurrence rates (fourth panel from the top) and b -value (fifth panel from the top) computed in the way described above in this section. The timescale is the same as the one used for the top panels related to the average stress and its standard deviation. Please note that the values plotted in the two bottom panels are computed from a set of 100 earthquakes preceding the time of computation. In this way, the variations are smoothed and do not appear as instantaneous steps. It can also be noted that the b -value plot appears rather noisy, due to the statistical uncertainty of the value obtained by only 100 earthquakes. However, we can observe a certain correlation between the occurrence rates and the

b -values. In general, high occurrence rates and high b -values correspond to high stress and vice versa. High occurrence rates and high b -values are generally notable in the decades preceding earthquakes of large magnitude, marked by red vertical lines. However, in some cases, the trend of increasing values stops and a decrease is notable immediately before the strong earthquakes.

As already stated in Section 2, we preferred to adopt a coefficient fc of 1.0 (full coupling) for the Nankai Trough fault system according to Sholz & Campos (2012). Actually, from the available literature listed in Section 2, it is not easy to choose the appropriate value for fc for each fault segment of the Nankai–Tokai system because this coefficient could be variable on different parts of a single segment.

In order to give an example of the results obtainable from a different choice of fc , we made an exercise using a coefficient equal to 0.5 in our simulator algorithm for segment A. The result, displayed in Fig. 4, shows that, in this case, the timescale is expanded

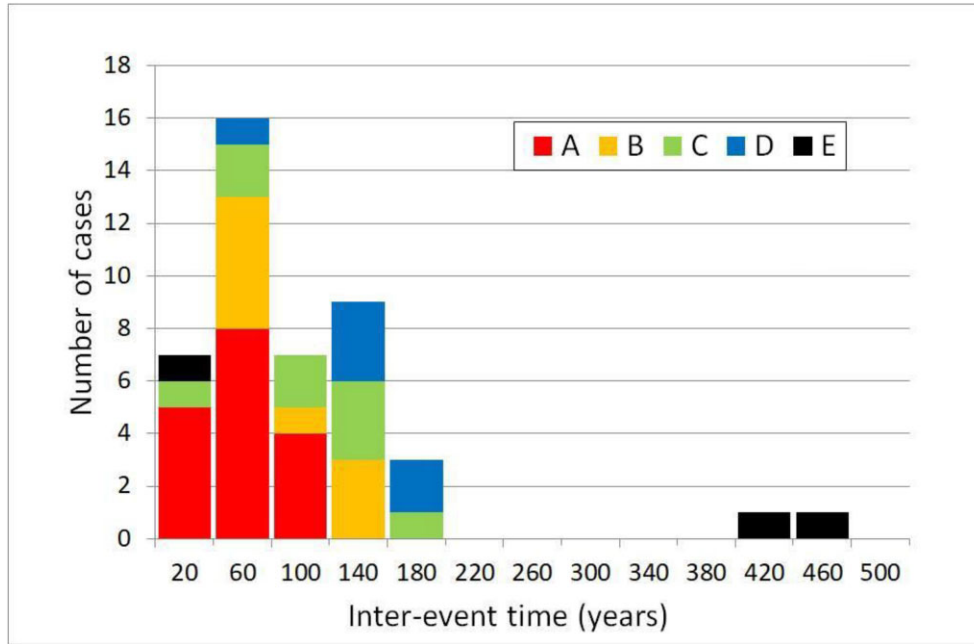


Figure 6. Inter-event time distribution in bins of 40 yr, for earthquakes of $M \geq 7.5$ from a simulation of 1000 yr of seismic activity across the five fault segments of the Nankai fault system. Each X-axis label shows the central value of the bin.

Table 4. Statistical parameters for earthquakes of $M \geq 7.5$ of the 1000 yr simulated catalogue of the five fault segments of the Nankai fault system.

Segment	Tr (yr)	Σ (yr)	C_v	$dlogL$
A	55.2	24.4	0.44	7.2
B	97.9	36.0	0.37	5.6
C	107.8	47.4	0.44	-2.2
D	146.9	33.0	0.22	4.2
E	293.8	193.5	0.66	-13.1

Notes. Tr : mean inter-event time; Σ : standard deviation; C_v : coefficient of variation and $dlogL$: the difference between the log-likelihood computed by the b and the Poisson time-independent model.

by a factor of two on the output catalogue with respect to the case of $fc = 1.0$.

For a better analysis of the temporal variations of the occurrence rates and the b -values shown in Fig. 3, we adopt the stacking technique earlier introduced by Console *et al.* (2018, 2024). By this method, we analyse the seismic activity before and after pivot earthquakes with magnitude $\geq M_{pivot}$ (in this case $M_{pivot} = 5.8$). For each earthquake of this magnitude, we examine the catalogue for a time period T_{dur} (here $T_{dur} = 20$ yr) before and after the pivot earthquake, dividing these periods into bins of length T_{bin} (here $T_{bin} = 0.2$ yr). Earthquakes within the same bin were included if their epicentres were within a distance R_{dist} (here $R_{dist} = 50$ km) from the pivot earthquake and their magnitudes were above M_{min} (here $M_{min} = 5.1$). This process was repeated for all such earthquakes, and the earthquakes in each bin were counted together.

Fig. 5 shows that, on average, the simulated catalogue contains a gradual increase of seismic activity in the period of 20 yr before the pivot earthquakes, but a sudden decrease occurs 2 yr before these large earthquakes. For the b -value, we note an increase starting 5 yr before the pivot earthquakes, and a decrease about 6 months before them. The increase in b -values accompanied by an increase in occurrence rates denotes that the number of small magnitude earthquakes is increasing faster than that of

the larger magnitude ones. This trend is interrupted a few months before the pivot earthquakes, when the occurrence rate is decreasing and the seismic activity concentrates on large earthquakes, in connection with the increasing size of the rupturing asperities. See Console *et al.* (2024) for a deeper analysis of these phenomena.

4.3. Statistical analysis of the inter-event times

We carried out a statistical analysis of the inter-event times for the 1000-yr simulation of the seismicity in the Nankai fault system. According to the ‘Ellsworth B’ equation (WGCEP 2003), the magnitude of earthquakes rupturing the entire area of one of the segments labelled from A to E would range from 8.2 to 8.6 (comparable with those reported in Table 1). In this study, we considered the statistics of earthquakes capable of rupturing a relevant part of one or more of these segments, even if they are smaller than the magnitude corresponding to the rupture of an entire segment. An earthquake is assigned to a segment if the following conditions are fulfilled: its magnitude is at least 7.5 and the nucleation is located on that segment or the area ruptured by the earthquake on that segment is equal to or greater than 50 per cent of the area of the entire segment.

Fig. 6 shows the distribution of inter-event times in the simulation. In this figure, we may see that the most typical inter-event time for the most active segments (A and B) is between 40 and 80 yr, while for segments C and D, it is 140 yr. This feature is consistent with the historical record (Table 1), considering that we are now examining earthquakes with a magnitude threshold smaller by 0.5 mag units.

Table 4 displays the mean inter-event time, the standard deviation and the coefficient of variation for each fault segment. The relatively short average inter-event times of the simulations can be justified by the circumstance that often two or more segments rupture simultaneously in a single earthquake, considering

also that two earthquakes close in time may rupture different parts of the same segment. This is the case, for instance, of the short inter-event time of 20 yr for segment E. Along with the above-mentioned temporal parameters, Table 4 also reports the results of the difference between the log-likelihood computed by the Brownian Passage Time renewal model and the Poisson time-independent model ($d\log L$). For the likelihood estimation, we have adopted the values obtained for T_r and C_v reported in Table 4 for each fault segment.

Both Fig. 6 and Table 4 show, as expected, that the most active segments are those characterized by higher slip rates (segments A, B and C). The simulation also shows that for the less active segments (segment E) inter-event times larger than 400 yr are possible. The coefficient of variation C_v is typically close to 0.4, which can be associated to a remarkably time-predictable behaviour of the seismicity. The positive log-likelihood difference ($d\log L$) denotes a better performance of the renewal model against the time-independent hypothesis only for three of the five segments. This is justified, *inter-alia*, by the modest number of earthquakes in a sample of just 1000 yr.

The behaviour of a time-predictable model resulting from our simulations is also clearly visible in the time history of stress shown in the top panels of Fig. 3. The preference for the time-predictable model in our study region was first supported by Shimazaki & Nakata (1980), even if other studies underlined more complicated features in a more general plate boundary context (see e.g. Thatcher 1984; Schwartz 1999).

Our results can be compared with those obtained by Meade (2023), who used a 3-D non-planar model of the Nankai subduction zone fault system to generate a simulated earthquake sequence over a 1250-yr-long interval, including 700 + M_w 5.5–8.5 earthquakes, with decadal-to-centennial scale quiescent intervals of quasi-periodic great earthquake clusters followed by aftershock sequences. Despite the relevant differences between the approaches adopted by our and his studies (physical versus probabilistic, and planar versus 3-D), the most notable of which is the G-R law imposed by Meade (2023) rather than the physics-based magnitude distribution produced by our algorithm, we obtained impressive similarities in periodicity and inter-event times of strong earthquakes of our respective catalogues. Due to the difference in our and Meade's approaches, we may note also some differences in the respective results, one difference is, for instance, the fact that the Meade's simulated catalogue displays much more Omori's law like aftershocks sequences than our results derived only from a self-organized physical system.

5 CONCLUSIONS

The main aim of this study was to achieve a better comprehension and possible predictability of the seismic process by the simulation performed through an algorithm based on well-constrained modelling of the causative sources of large earthquakes. The principal concept on which the simulator is built consists simply of the stress-rebound theory introduced by Reid (1910). In the recent development of earthquake simulators, this theory is generalized to ruptures of any size, as previously described in the Introduction and in the methods section more in detail.

Interesting seismic features are evidenced by the results of our simulator applied to the Nankai megathrust fault system. Focusing on the long-term behaviour of the seismic process on single fault segments, we noted the following features (Figs 3 and 5):

- as expected, stress always increases with tectonic loading and suddenly decreases during major earthquakes;
- since major earthquakes consistently occur when stress reaches an almost constant value on the fault segment containing the nucleation point, a 'time predictable model' behaviour of the seismic cycle is supported, as opposed to the 'slip predictable model' model;
- the stress standard deviation always increases immediately after major earthquakes, tends to remain constant for a while, and then decreases more and more rapidly as the next major earthquake approaches;
- parameters such as occurrence rate and b -value, which are seismologically observable, are correlated to stress and its standard deviation, as potential precursors of large magnitude earthquakes;
- in this context, in the simulated catalogue major earthquakes mostly occur during periods of high seismic activity and are followed by periods of quiescence;
- the b -value of the simulated seismic activity tends to increase before major earthquakes and exhibits a correlation with occurrence rate, even if an opposite trend is often noted shortly before strong earthquakes;
- fault segmentation of our model does not significantly limit the growth of a rupture, which can expand from one segment to another, producing a continuous magnitude distribution even in the large magnitudes range, rather than characteristic magnitudes only.

Even if our study was aimed to explore methodological aspects and potential capabilities of new-generation simulator algorithms, these results encourage further investigations about the application of simulators in support of other methodologies of time-independent and time-dependent seismic hazard assessment.

DATA AVAILABILITY

The simulated catalogue mentioned in this manuscript is available upon request to the authors.

ACKNOWLEDGMENTS

The authors thank the editor Dr M. Segou, Dr E.E. Papadimitriou and two anonymous reviewers for their support and valuable suggestions to improve our manuscript.

REFERENCES

- Ando, M., 1975a. Possibility of a major earthquake in the Tokai district, Japan, and its pre-estimated seismotectonic effects, *Tectonophysics*, **25**, 69–85.
- Ando, M., 1975b. Source mechanisms and tectonic significance of historical earthquakes along the Nankai trough, Japan, *Tectonophysics*, **27**, 119–140.
- Araki, E., Saffer, D.M., Kopf, A.J., Wallace, L.M., Kimura, T., Machida, Y., Ide, S. & Davis, E., IODP Expedition 365 shipboard scientists, 2017. Recurring and triggered slow-slip events near the trench at the Nankai Trough subduction megathrust, *Science*, **356**(6343), 1157–1160.
- Baba, T. & Cummins, P.R., 2005. Contiguous rupture areas of two Nankai Trough earthquakes revealed by high-resolution tsunami waveform inversion, *Geophys. Res. Lett.*, **32**, doi:10.1029/2004GL022320.
- Christophersen, A., Rhoades, D.A. & Colella, H.V., 2017. Precursory seismicity in regions of low strain rate: insights from a physics-based earthquake simulator, *Geophys. J. Int.*, **209**, 1513–1525.

- Console, R. & Carluccio, R., 2021. Earthquake simulators development and application, In: *Statistical Methods and Modeling of Seismogenesis*, ISTE, Wiley, pp. 27–58.
- Console, R. & Murru, M., 2001. A simple and testable model for earthquake clustering, *J. geophys. Res.*, **106**, 8699–8711.
- Console, R., Carluccio, R. & Vannoli, P., 2024. Simulated seismicity as a tool for studying the long-term seismogenic process: an Italy–Japan comparison, *Appl. Sci.*, **14**, 17, doi :10.3390/app14177900.
- Console, R., Carluccio, R., Murru, M., Papadimitriou, E. & Karakostas, V., 2022a. Physics-based simulation of spatiotemporal patterns of earthquakes in the Corinth Gulf, Greece, fault system, *Bull. seism. Soc. Am.*, **112**, 98–117.
- Console, R., Carluccio, R., Papadimitriou, E. & Karakostas, V., 2015. Synthetic earthquake catalogs simulating seismic activity in the Corinth Gulf, Greece, fault system, *J. geophys. Res.: Solid Earth*, **120**, 326–343.
- Console, R., Murru, M. & Lombardi, A.M., 2003. Refining earthquake clustering models, *J. geophys. Res.*, **108**, 2468, doi :10.1029/2002JB002130.
- Console, R., Murru, M., Vannoli, P., Carluccio, R., Taroni, M. & Falcone, G., 2020. Physics-based simulation of sequences with multiple main shocks in Central Italy, *Geophys. J. Int.*, **223**, 526–542.
- Console, R., Vannoli, P. & Carluccio, R., 2018. The seismicity of the Central Apennines (Italy) studied by means of a physics-based earthquake simulator, *Geophys. J. Int.*, **212**, 916–929.
- Console, R., Vannoli, P. & Carluccio, R., 2022b. Physics-based simulation of sequences with foreshocks, aftershocks and multiple main shocks in Italy, *Appl. Sci.*, **12**, 2062, doi:10.3390/app12042062.
- Console, R., Vannoli, P. & Carluccio, R., 2023. The 2022 seismic sequence in the Northern Adriatic Sea and its long-term simulation, *Appl. Sci.*, **13**, 6, doi:10.3390/app13063746.
- DeMets, C., Gordon, R.G. & Argus, D.F., 2010. Geologically current plate motions, *Geophys. J. Int.*, **181**(1), 1–80.
- Dieterich, J., 1994. A constitutive law for rate of earthquake production and its application to earthquake clustering, *J. geophys. Res.*, **99**(B2), 2601–2618.
- Field, E.H., 2015. Computing elastic-Rebound-motivated earthquake probabilities in unsegmented fault models: a new methodology supported by physics-based simulators, *Bull. seism. Soc. Am.*, **105**(2A), 544–559.
- Field, E.H., 2019. How physics-based earthquake simulators might help improve earthquake forecasts, *Seismol. Res. Lett.*, **90**(2A), 467–472.
- Fitzenz, D.D., 2018. Conditional probability of what? Example of the Nankai interface in Japan, *Bull. seism. Soc. Am.*, **108**, 3169–3179.
- Fujiwara, O., Goto, K., Ando, R. & Garrett, E., 2023. Paleotsunami research along the Nankai Trough and Ryukyu Trench subduction zones—current achievements and future challenges, *Earth Sci. Rev.*, **210**, 103333, doi: 10.1016/j.earscirev.2020.103333.
- Gulia, L. & Wiemer, S., 2019. Real-time discrimination of earthquake foreshocks and aftershocks, *Nature*, **574**, 193–199.
- Gulia, L., Tormann, T., Wiemer, S., Hermann, M. & Seif, S., 2016. Short-term probabilistic earthquake risk assessment considering time-dependent b-values, *Geophys. Res. Lett.*, **43**, 1100–1108.
- International Seismological Centre, 2024. On-line Bulletin, <https://doi.org/10.31905/D808B830> (Accessed 02 May 2024).
- Ishibashi, K., 1981. *Specification of a Soon-to-occur Seismic Faulting in the Tokai District, Central Japan, based upon Seismotectonics. Maurice Ewing Series 4*. American Geophysical Union, Washington, DC, pp. 297–332.
- Kanamori, H., 1972. Tectonic implications of the 1944 Tonankai and the 1946 Nankaido earthquakes, *Phys. Earth planet. Inter.*, **5**, 129–139.
- Kato, T., 1983. High-angle reverse faulting associated with the 1946 Nankaido earthquake, *Tectonophysics*, **93**, 31–44.
- Meade, B.J., 2023. Kinematic earthquake sequences on geometrically complex faults, <https://arxiv.org/abs/2304.06797>.
- Montuori, C., Murru, M. & Falcone, G., 2016. Spatial variation of the b-value observed for the periods preceding and following the 24 August 2016, Amatrice earthquake (ML 6.0) (Central Italy), *Ann. Geophys.*, **59**, 5, doi:10.4401/ag-7273.
- Mosca, I., Console, R. & D’Addezio, G., 2012. Renewal models of seismic recurrence applied to paleoseismological and historical observations, *Tectonophysics*, **564–565**, 54–67.
- Nakano, M. et al. 2018a. The 2016 Mw 5.9 earthquake off the southeastern coast of Mie Prefecture as an indicator of preparatory processes of the next Nankai Trough megathrust earthquake, *Prog. Earth Planet Sci.*, **5**, doi: 10.1186/s40645-018-0188-3.
- Nakano, M., Hori, T., Araki, E., Kodaira, S. & Ide, S., 2018b. Shallow very-low-frequency earthquakes accompany slow slip events in the Nankai subduction zone, *Nat. Commun.*, **9**, 984, doi:10.1038/s41467-018-303431-5.
- Nanjo, K.Z. & Yoshida, A.A., 2018. B map implying the first eastern rupture of the Nankai Trough earthquakes, *Nat. Commun.*, **9**, 1117, doi: 10.1038/s41467-018-03514-3.
- Nanjo, K.Z., Yamamoto, Y., Ariyoshi, K. et al., 2024. Earthquake detection capacity of the Dense Oceanfloor Network system for Earthquakes and Tsunamis (DONET), *J. Seismol.*, **28**, 787–810.
- Noda, A., Saito, T., Fukuyama, E. & Urata, Y., 2021. Energy-based scenarios for great thrust-type earthquakes in the Nankai trough subduction zone, southwest Japan, using an interseismic slip-deficit model, *J. geophys. Res.: Solid Earth*, **126**, doi :10.1029/2020JB020417.
- Ogata, Y., 1998. Space-time point-process models for earthquake occurrences, *Ann. Inst. Stat. Math.*, **50**, 379–402.
- Parsons, T., Console, R., Falcone, G., Murru, M. & Yamashina, K., 2012. Comparison of characteristic and Gutenberg–Richter models for time-dependent $M \geq 7.9$ earthquake probability in the Nankai-Tokai subduction zone, Japan, *Geophys. J. Int.*, **190**, 1673–1688.
- Reid, H.F., 1910. *The Mechanics of the Earthquake, The California Earthquake of April 18, 1906, Report of the State Investigation Commission*, 2, Carnegie Institution of Washington, Washington, DC.
- Ruff, L. & Kanamori, H., 1983. Seismic coupling and uncoupling at subduction zones, *Tectonophysics*, **99**, 99–117.
- Rundle, J.B. & Brown, S., 1991. Origin of rate dependence in frictional sliding, *J. Stat. Phys.*, **65**, 403–412.
- Rundle, J.B. & Jackson, D.D., 1977. Numerical simulation of earthquake sequences, *Bull. seism. Soc. Am.*, **87**, 1363–1377.
- Rundle, J.B., Stein, S., Donnellan, A., Turcotte, D.L., Klein, W. & Cameron Saylor, C., 2022. The complex dynamics of earthquake fault systems: new approaches to forecasting and nowcasting of earthquakes, *Rep. Prog. Phys.*, **84**, 076801, doi:10.1088/1361-6633/abf893.
- Saito, T. & Noda, A., 2022. Mechanically coupled areas on the plate interface in the Nankai trough, Japan and a possible seismic and aseismic rupture scenario for megathrust earthquakes, *J. geophys. Res.: Solid Earth*, **127**, doi: 10.1029/2022JB023992.
- Scholz, C.H. & Campos, J., 2012. The seismic coupling of subduction zones revisited, *J. geophys. Res.*, **117**, B05310, doi:10.1029/2011JB009003.
- Schultz, K.W., Sachs, M., Yoder, M.R., Rundle, J.B., Turcotte, D.L., Helen, E.M. & Donnellan, A., 2015. in Virtual Quake: statistics, Co-seismic deformations and gravity changes for driven earthquake fault systems, pp.1–6, Hashimoto, M.eds, *International Symposium on Geodesy for Earthquake and Natural Hazards (GENAH)*, International Association of Geodesy Symposia, Vol. 145, Springer, Cham.
- Schwartz, S.Y., 1999. Noncharacteristic behavior and complex recurrence of large subduction zone earthquakes, *J. geophys. Res.: Solid Earth*, **104**(B10), 23111–23125.
- Shaw, B.E., Milner, K.R., Field, E.H., Richards-Dinger, K., Gilchrist, J.J., Dieterich, J.H. & Jordan, T.H., 2018. A physics-based earthquake simulator replicates seismic hazard statistics across California, *Sci. Adv.*, **4**, 8, doi: 10.1126/sciadv.aau0688.
- Shimazaki, K. & Nakata, T., 1980. Time-predictable recurrence model for large earthquakes, *Geophys. Res. Lett.*, **7**(4), 279–282.
- Stallone, A. & Marzocchi, W., 2019. Features of seismic sequences are similar in different crustal 384 tectonic regions, *Bull. seism. Soc. Am.*, **109**(5), 1594–1604.
- Sykes, L.R. & Menke, W., 2006. Repeat times of large earthquakes: implications for earthquake mechanics and long-term prediction, *Bull. seism. Soc. Am.*, **96**(5), 1569–1596.

- Thatcher, W., 1984. The earthquake deformation cycle, recurrence, and the time-predictable model, *J. geophys. Res.: Solid Earth*, **89**(B7), 5674–5680.
- Tormann, T., Wiemer, S. & Mignan, A., 2014. Systematic survey of high-resolution b value imaging along Californian faults: inference on asperities, *J. geophys. Res.*, **119**, 2029–2054.
- Tullis, T.E., 2012. Generic earthquake simulator. Preface to the focused issue on earthquake simulators, *Seismol. Res. Lett.*, **83**(6), 957–958.
- Ward, S.N., 1992. An application of synthetic seismicity in earthquake statistics: the Middle America trench, *J. geophys. Res.*, **97**(B5), 6675–6682.
- Ward, S.N., 1996. A synthetic seismicity model for southern California: cycles, probability and hazard, *J. geophys. Res.*, **101**(B10), 2293–22418.
- Ward, S.N., 2000. San Francisco Bay Area earthquake simulations: a step towards a standard physical earthquake model, *Bull. seism. Soc. Am.*, **90**(2), 370–386.
- Ward, S.N., 2012. ALLCAL earthquake simulator, *Seismol. Res. Lett.*, **83**(6), 964–972.
- WGCEP, 2003. Earthquake Probabilities in the San Francisco Bay Region: 2002–2031. *U. S. Geological Survey*, Open-File Report 03-214.
- Wilson, J.M., Yoder, M.R., Rundle, J.B., Turcotte, D.L. & Schultz, K.W., 2017. Spatial evaluation and verification of earthquake simulators, *Pure appl. Geophys.*, **174**, 2279–2293.
- Yamamoto, Y., Yada, S., Ariyoshi, K., Hori, T. & Takahashi, N., 2022. Seismicity distribution in the Tonankai and Nankai seismogenic zones and its spatiotemporal relationship with interplate coupling and slow earthquakes, *Prog. Earth Planet. Sci.*, **9**, 32, doi :10.1186/s40645-022-00493-4.
- Yokota, Y., Ishikawa, T., Watanabe, S., Tashiro, T. & Asada, A., 2016. Seafloor geodetic constraints on interplate coupling of the Nankai Trough megathrust zone, *Nature*, **534**, 374–377.
- Yokota, Y. & Ishikawa, T., 2020. Shallow slow slip events along the Nankai Trough detected by GNSS-A. *SCIENCE ADVANCES*, **6**(3), eaay5786, doi:10.1126/sciadv.aay5786.
- Zang, S.X., Chen, Q.Y., Ning, J.Y., Shen, Z.K. & Liu, Y.G., 2002. Motion of the Philippine Sea plate consistent with the NUVEL-1A model, *Geophys. J. Int.*, **150**, 809–819.

APPENDIX A

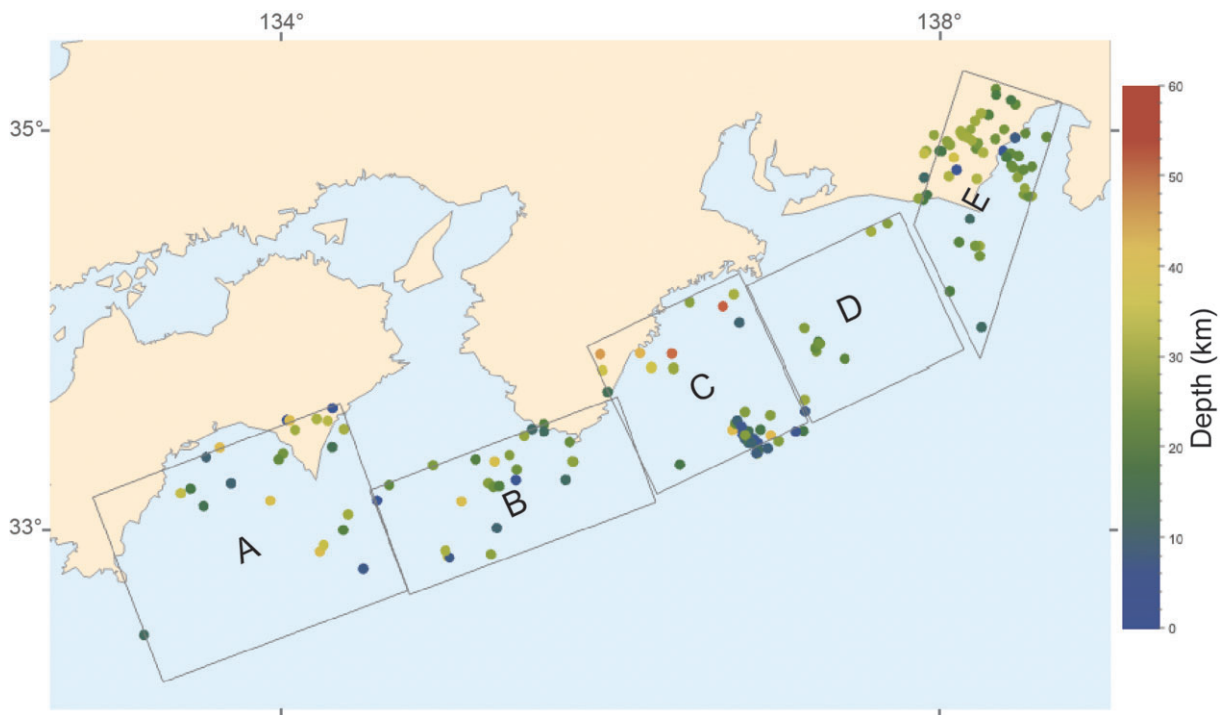


Figure A1. Map of the earthquakes of $M4.0+$ reported in the International Seismological Centre (2024) earthquake catalogue since 1970, for the region containing the fault system considered in our study.

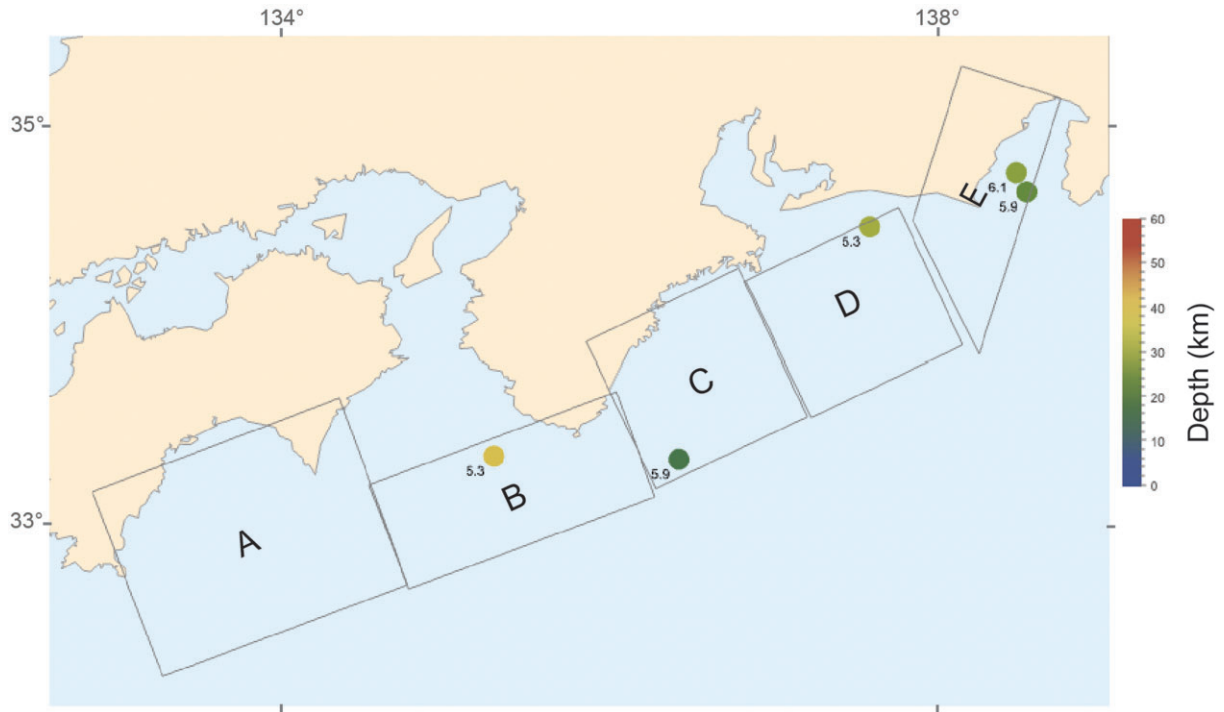


Figure A2. Map of the earthquakes of $M5.2+$ reported in the International Seismological Centre (2024) earthquake catalogue since 1970, for the region containing the fault system considered in our study.